Supporting Information

Investigation of Polyacrylic Acid as Universal Aqueous Binder for Ni-rich Cathodes and Si Anodes in Full cell Lithium-ion Batteries

Buket Boz[a*], Katja Fröhlich[a], Lukas Neidhart[a], Palanivel Molaiyan[a], Giovanni Bertoni[b], Marco Ricci[c,d], Francesco De Boni[c], Miljana Vuksanovic[a], Martina Romio[a], Karin Whitmore[e], Marcus Jahn[a]

[a] Battery Technologies, AIT Austrian Institute of Technology GmbH, Giefingasse 2, 1210 Vienna, Austria
[b] Consiglio Nazionale delle Ricerche Modena S3 via Campi 213/A 41125 Modena, Italy
[c] Italian Institute of Technology, Center for Convergent Technologies, Delta Lab, Via Morego 30, Genova, Italy
[d] Department of Chemistry and Industrial Chemistry, University of Genova, via Dodecaneso 31, Genova, 16146, Italy
[e] TU Wien, Universitäre Serviceeinrichtung für Transmissions-Elektronenmikroskopie, Wiedner Hauptstraße 8-10/057-02 1040 Vienna, Austria
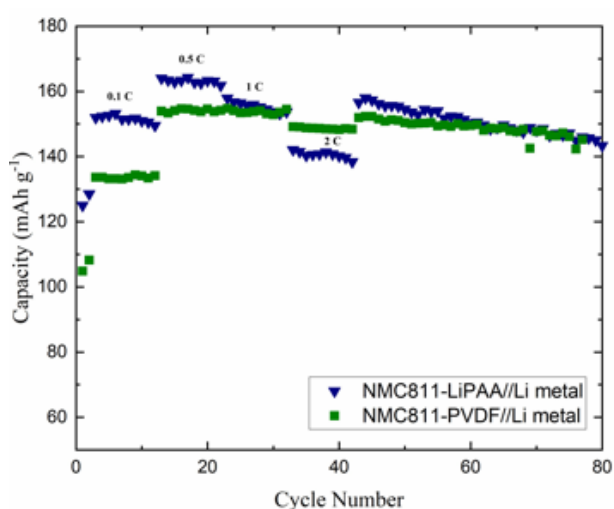*Corresponding Author: buket.boz@ait.ac.at

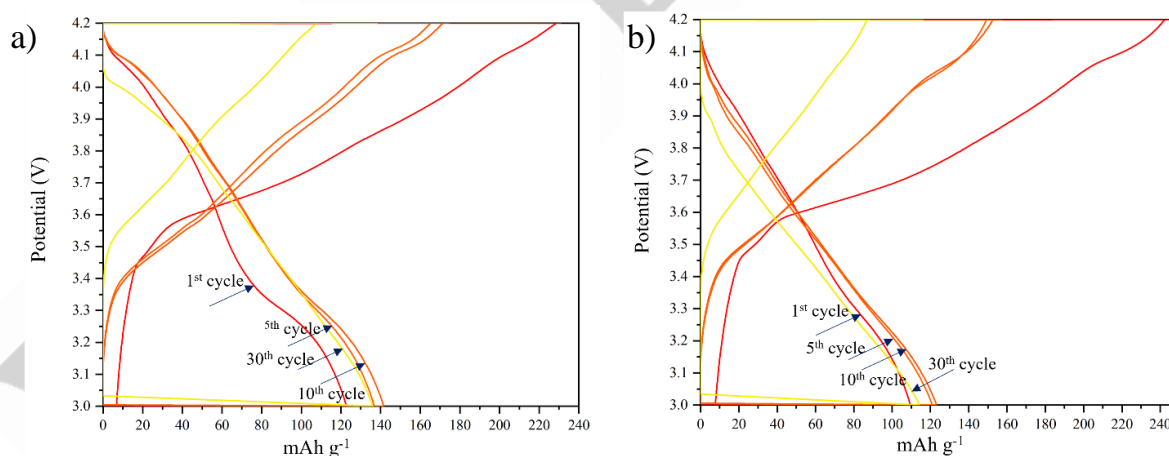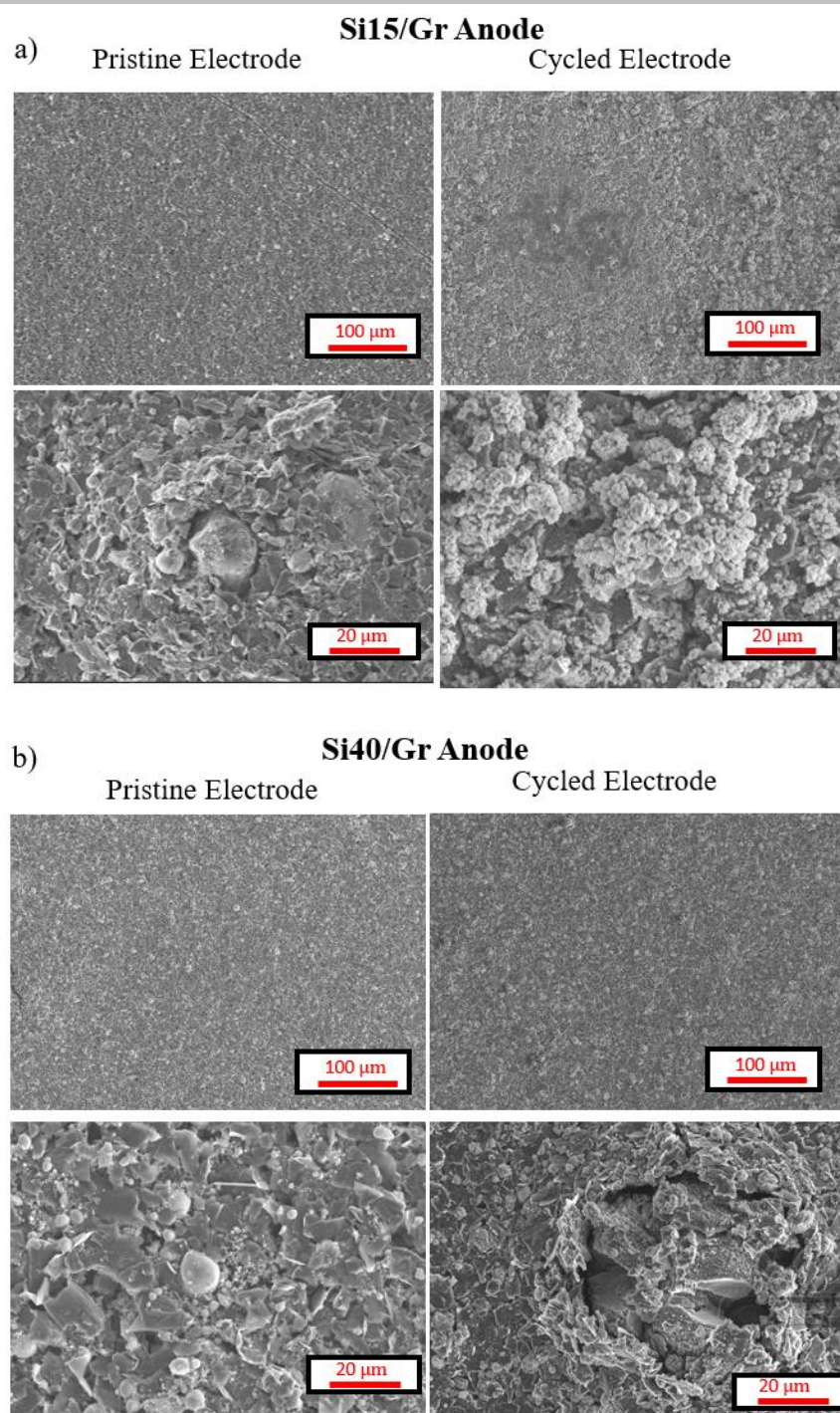**Figure S1.** Li metal//NMC811-LiPAA vs Li metal//NMC811-PVDF.

Figure S2. Discharge curves of Si15/Gr//NMC811-LiPAA and Si40/Gr//NMC811-LiPAA for the 1st, 5th, 10th and 30th cycles.

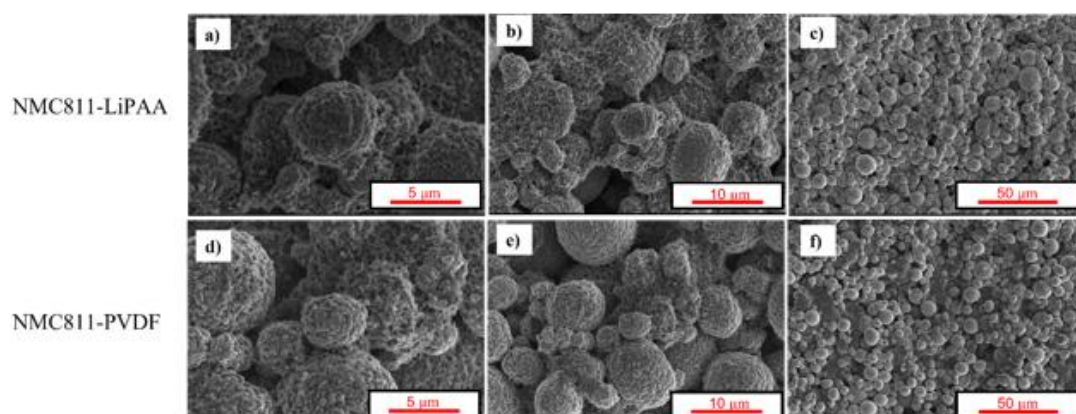**Figure S3.** SEM surface images of a) Si15/Gr before and after cycling and b) Si40/Gr before and after cycling.

Figure S4. SEM images of surface of the pristine cathodes at different scales a), b), c) NMC811-LiPAA d), e), f) NMC811-PVDF.
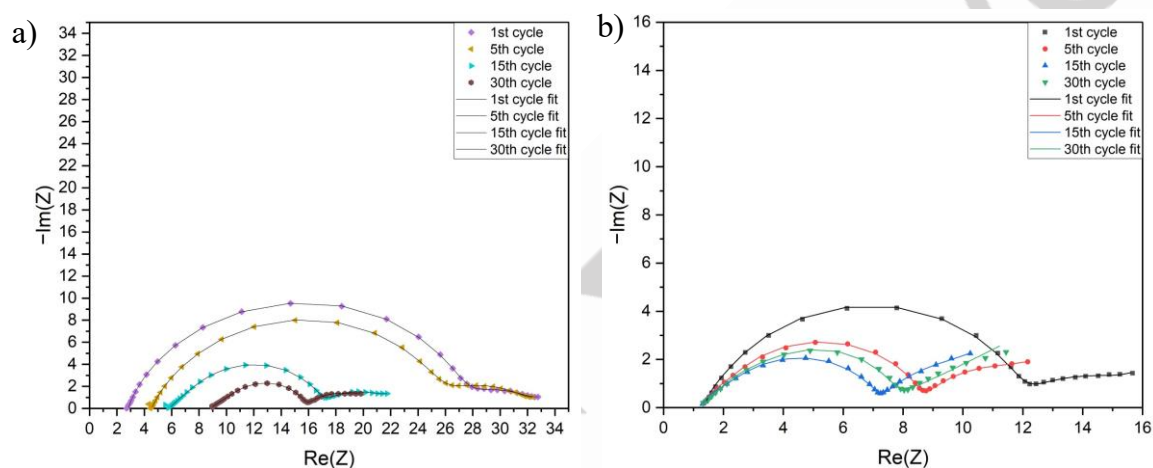

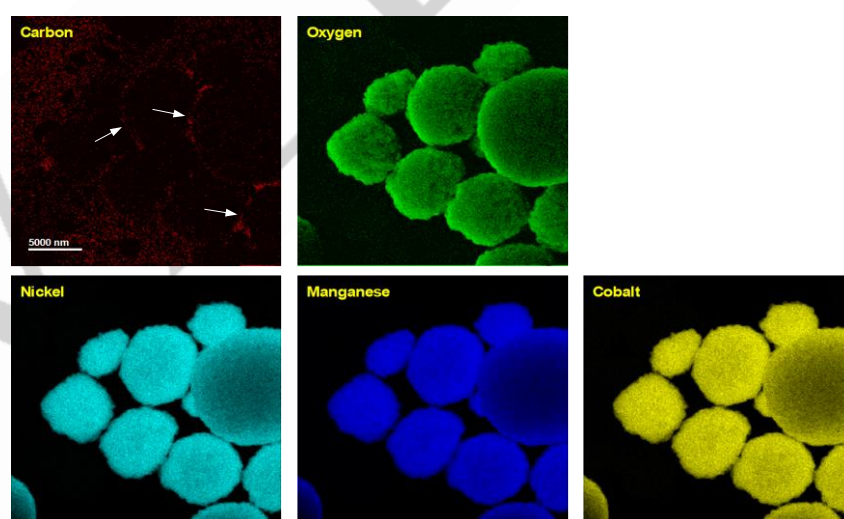**Figure S5.** EIS spectra of a) Si15 anode and b) Si40 anodes respectively.

Figure S6. EDXS maps from the NMC811 mixed cathode slurry.

No evidence of phase separation was found by looking at the transition metals Ni, Mn, and Co. Moreover, a signal from carbon was detected at the edges of the particles or aggregates of NMC811 (indicated by the white arrows), confirming the presence of the polymer at the surface. The noise in the carbon map is due to the support holey film of the TEM grid, also made of carbon.
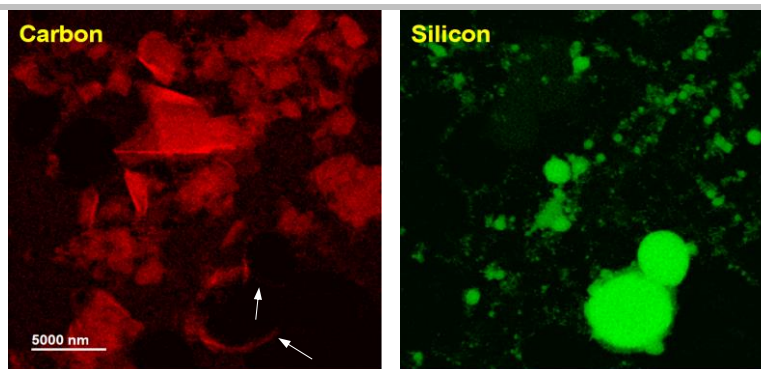
Figure S7. EDXS maps from the anode slurry (40% Si/Gr is presented for a higher concentration of Si particles in the map).

Carbon signal derives from both graphite and carbon black added in the mix. However, in this case, a small signal at the edges of the particles indicated the presence of the polymer (indicated by the white arrows).
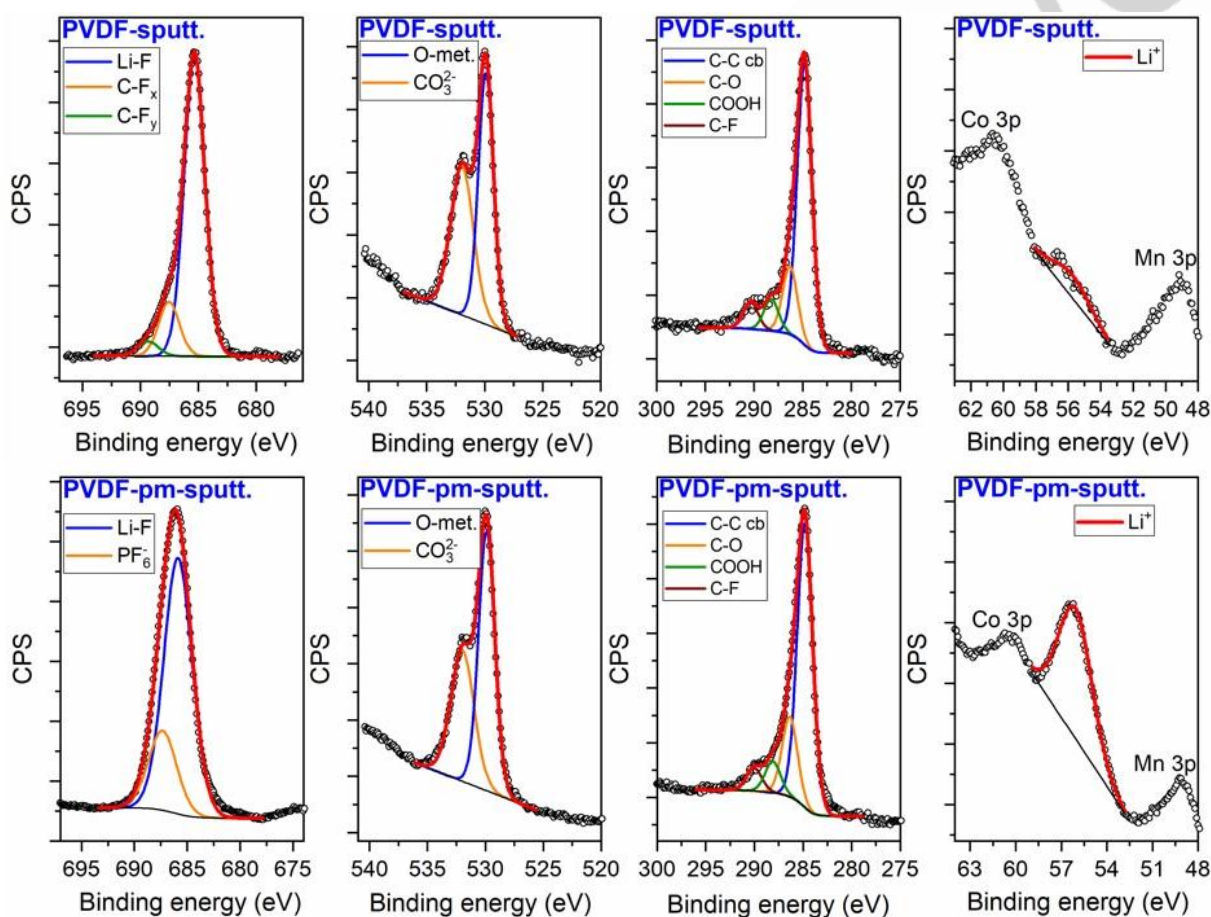

Figure S8. Comparison between high-resolution F 1s, O 1s, C 1s, and Li 1s XPS spectra of pristine NMC811-PVDF (PVDF-sputt.) and cycled (post mortem) NMC811-PVDF (PVDF-pm-sputt.) cathodes after sputtering.

The Li 1s region also contains two features due to Co 3p and Mn 3p peaks, respectively, which however don't overlap with Li 1s peak.
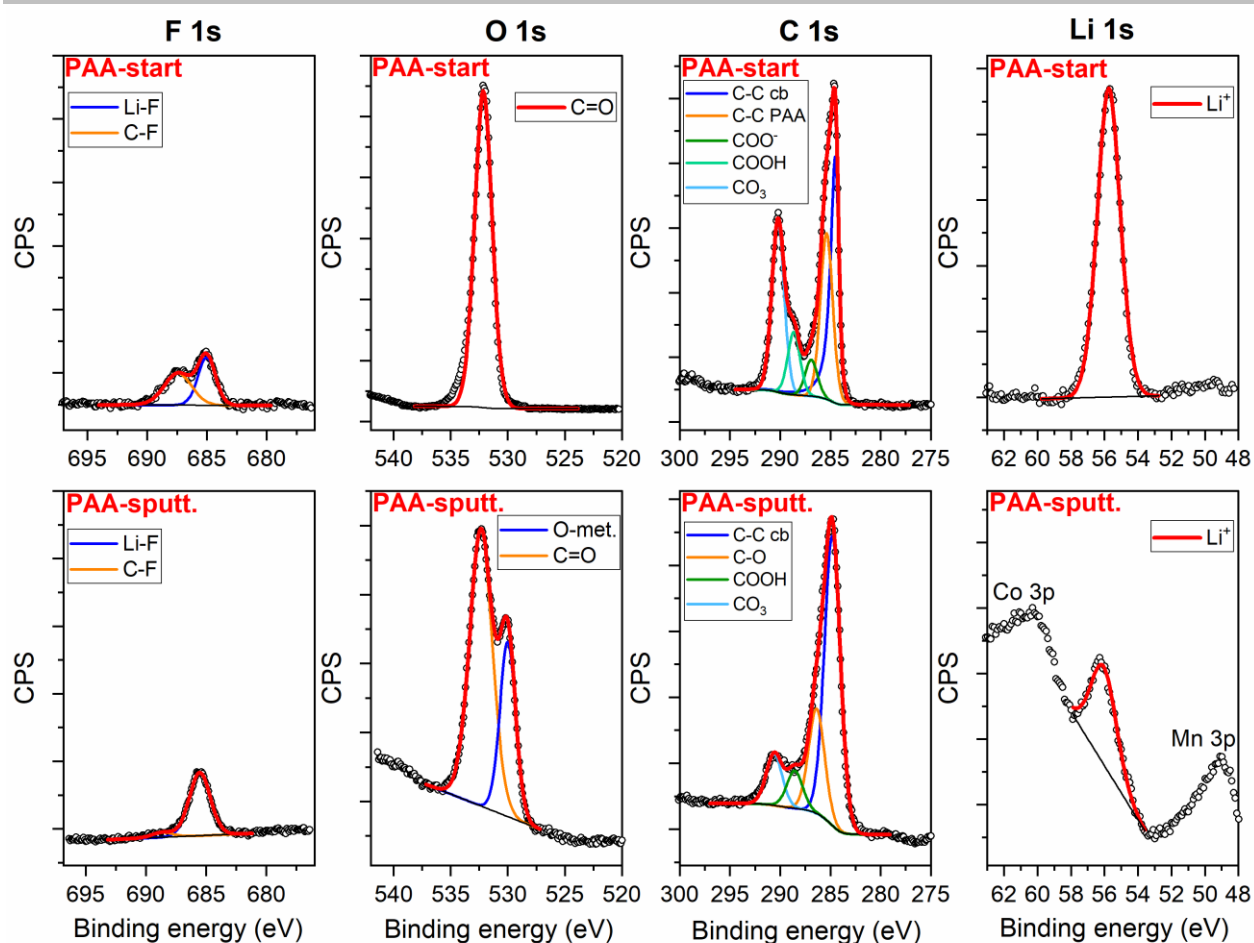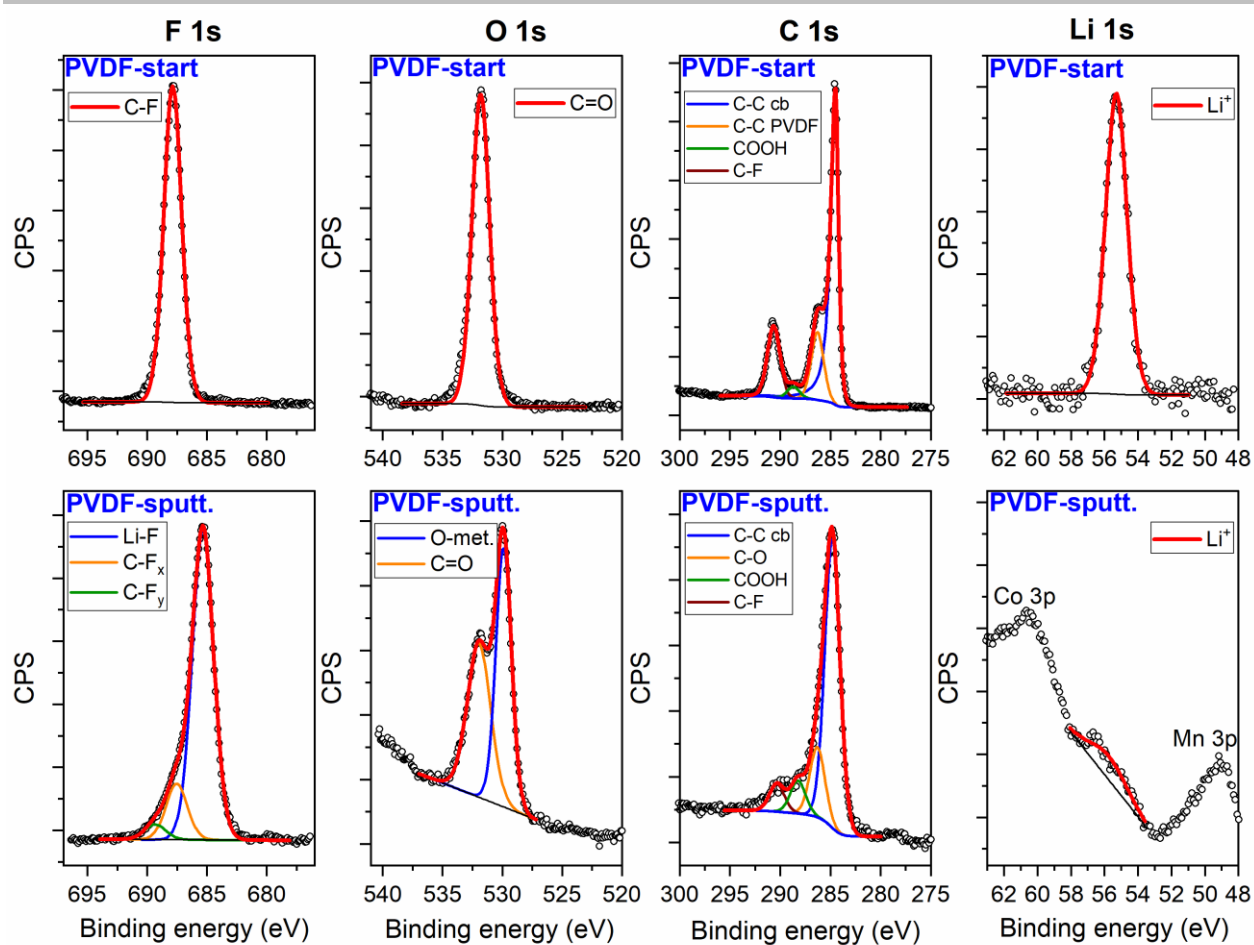
Figure S9. High-resolution XPS spectra of the PAA pristine sample before (PAA-start) and after (PAA-sputt.) sputtering and their corresponding elemental peak deconvolution of F 1s, O 1s, C 1s, and Li 1s.

The Li 1s region after sputtering also contains two features due to Co 3p and Mn 3p peaks, respectively, which however do not overlap with Li 1s peak.
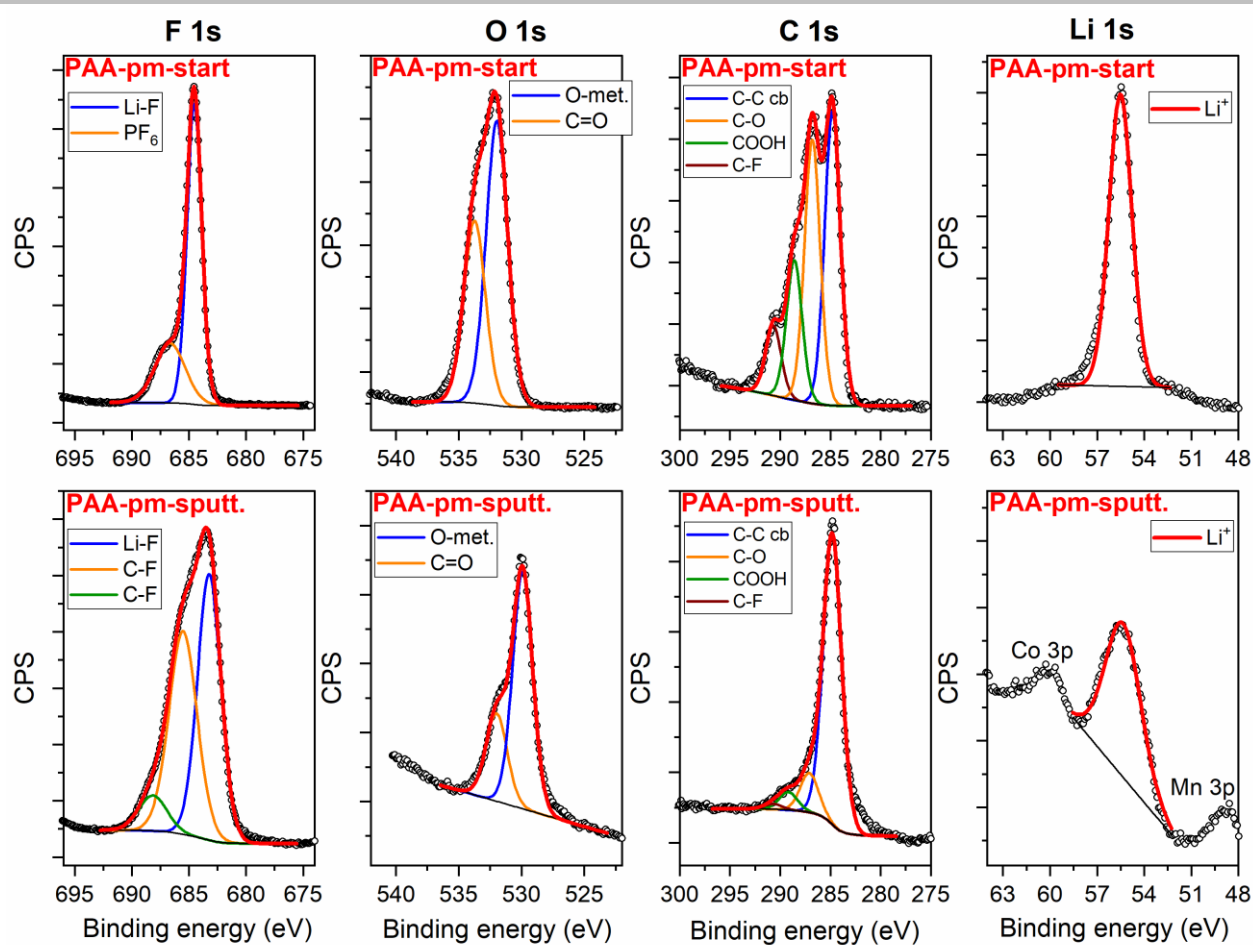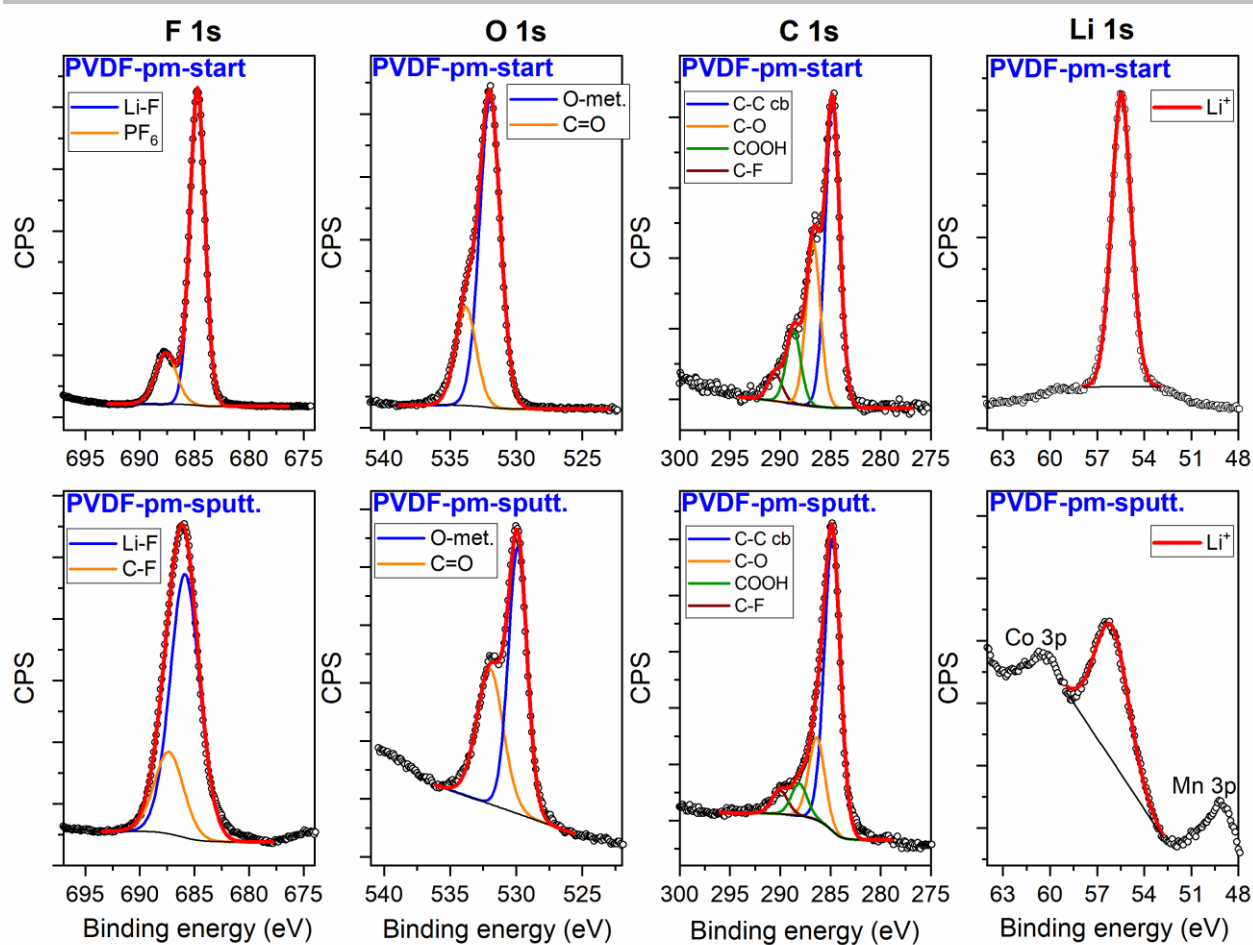
Figure S10. High-resolution XPS spectra of the PAA post-mortem sample before (PAA-pm-start) and after (PAA-pm-sputt.) sputtering and their corresponding elemental peak deconvolution of F 1s, O 1s, C 1s, and Li 1s.

The Li 1s region after sputtering also contains two features due to Co 3p and Mn 3p peaks, respectively, which however do not overlap with Li 1s peak.

Figure S11. High-resolution XPS spectra of the PVDF pristine sample before (PVDF-start) and after (PVDF-sputt.) sputtering and their corresponding elemental peak deconvolution of F 1s, O 1s, C 1s, and Li 1s.

The Li 1s region after sputtering contains two features due to Co 3p and Mn 3p peaks, respectively, which however do not overlap with Li 1s peak.

Figure S12. High-resolution XPS spectra of the PVDF post-mortem sample before (PVDF-pm-start) and after (PVDF-pm-sputt.) sputtering and their corresponding elemental peak deconvolution of F 1s, O 1s, C 1s, and Li 1s.

The Li 1s region after sputtering also contains two features due to Co 3p and Mn 3p peaks, respectively, which however do not overlap with Li 1s peak.

8
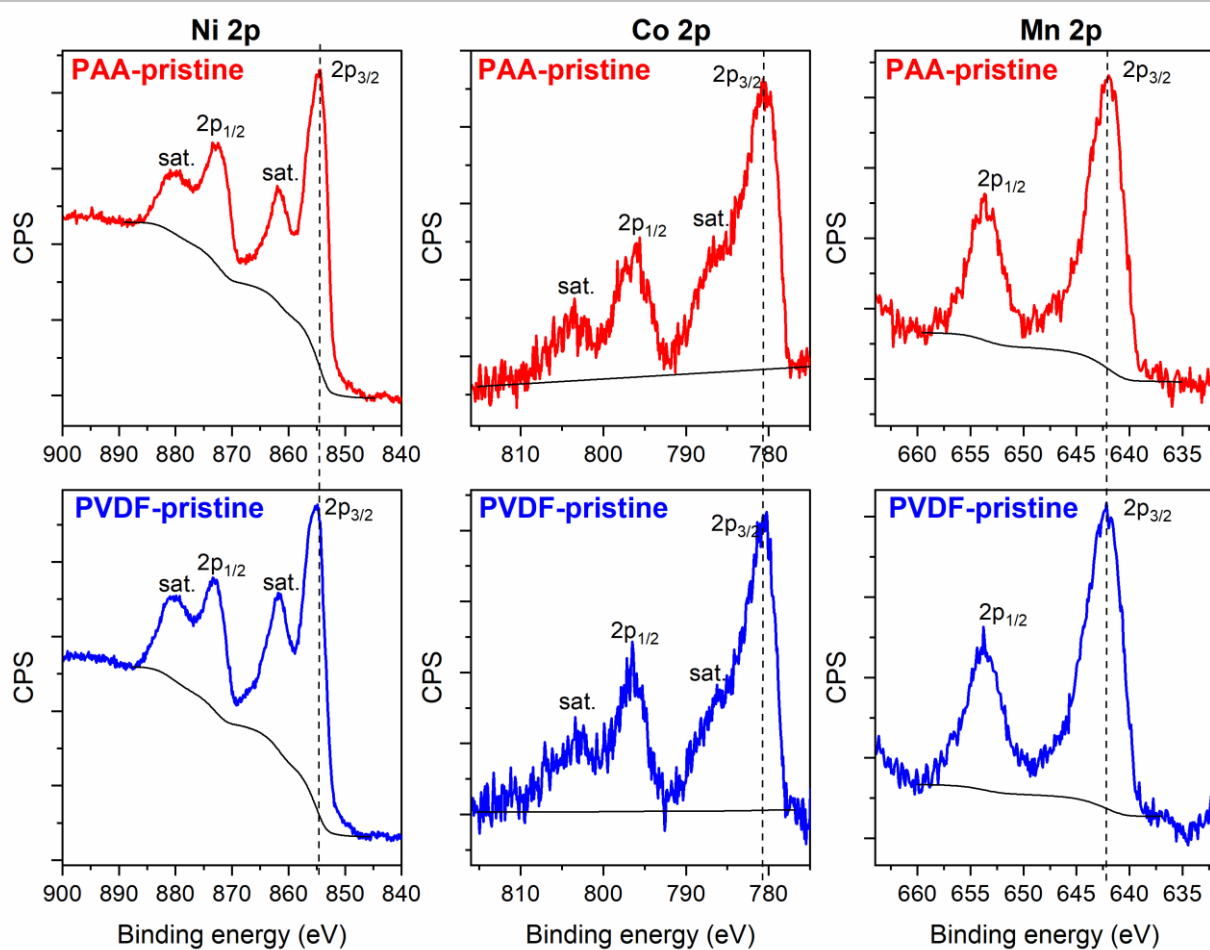
Figure S13. High-resolution XPS spectra of Ni 2p, Co 2p, and Mn 2p regions of the two analyzed pristine cathodes. The position of the $2p_{3/2}$ component is highlighted by a dash line in each spectrum. The Mn 2p peak overlaps with a feature of the fluorine KLL Auger structure around 645 eV.

The contribution of the Auger structure was separated from the Mn 2p peak according to the method explained in the Materials & Methods Section. The result of such procedure is shown in Figure S12.
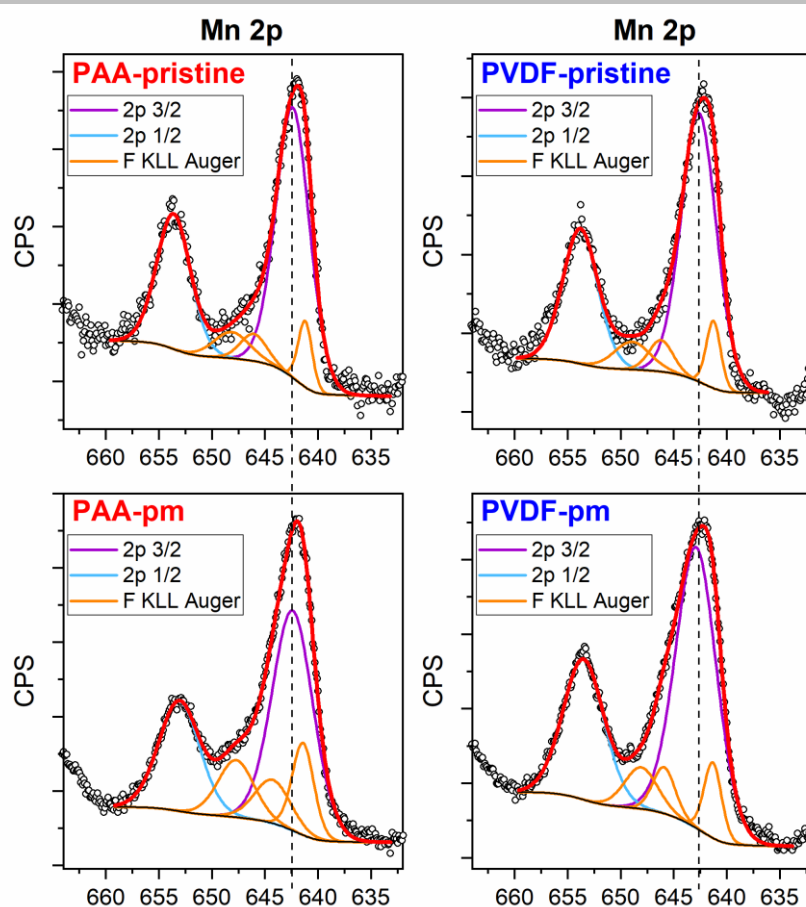
Figure S14. Deconvolution of the high-resolution Mn 2p region of the four analyzed samples. The fit was performed to separate the contribution of the fluorine KLL Auger structure around 645 eV from the Mn 2p peak, according to the method explained in the Materials & Methods Section in the main text.
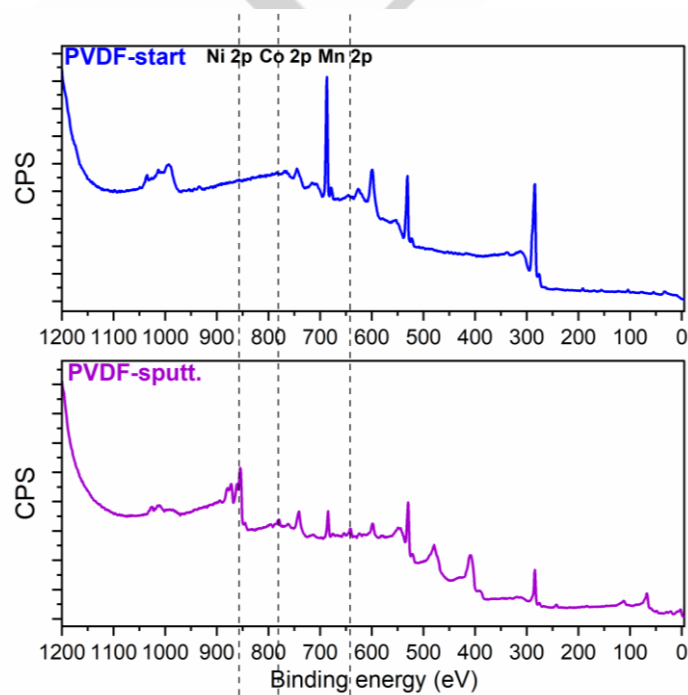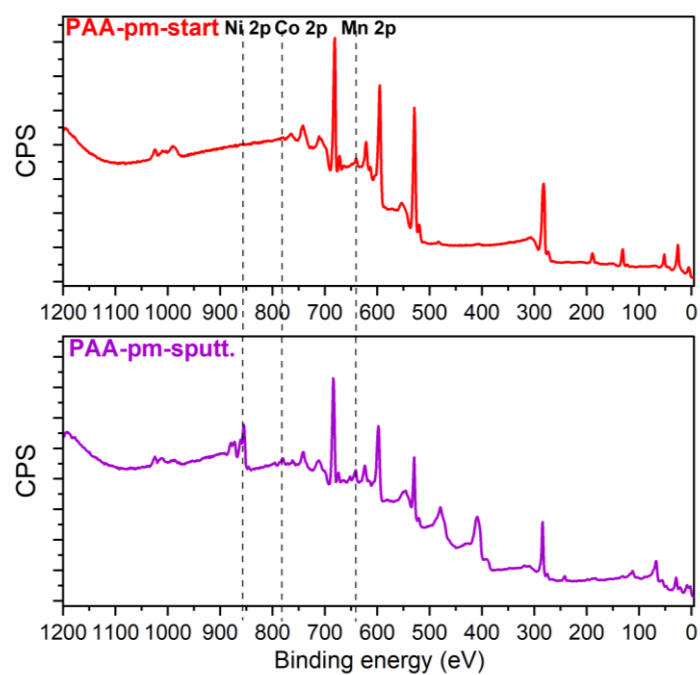

Figure S15. XPS wide scans of the PVDF pristine sample before (PVDF-start) and after (PVDF-sputt.) sputtering. The positions of Ni 2p, Co 2p, and Mn 2p peaks are highlighted by dash lines in each spectrum.

10
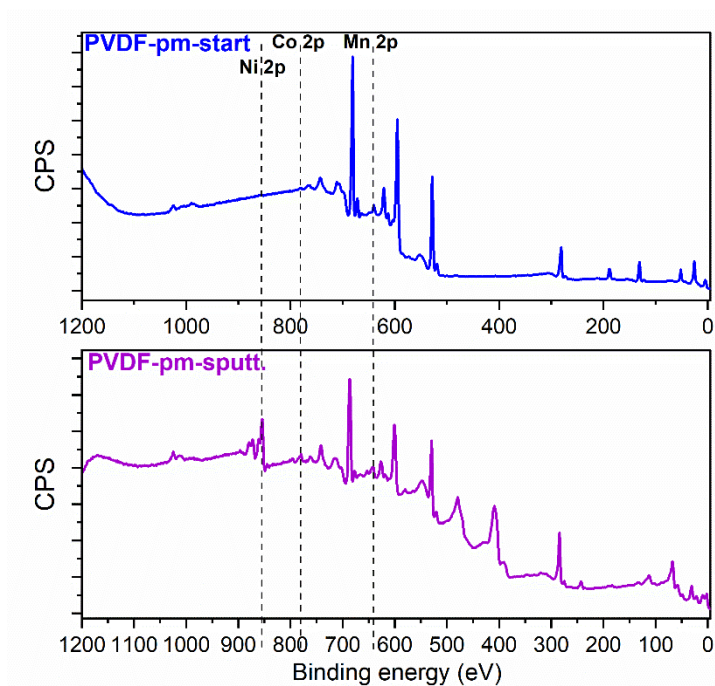
Figure S16. XPS wide scans of the PVDF post-mortem sample before (PVDF-pm-start) and after (PVDF-pm-sputt.) sputtering. The positions of Ni 2p, Co 2p, and Mn 2p peaks are highlighted by dash lines in each spectrum.
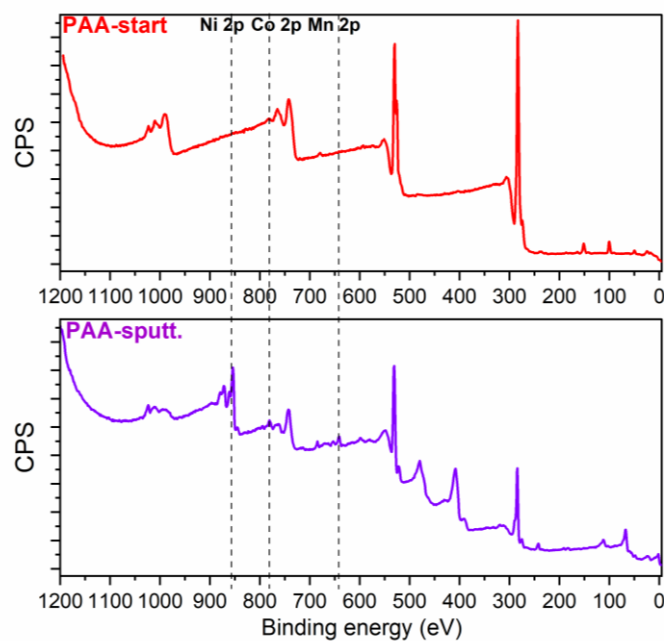
Figure S17. XPS wide scans of the PAA pristine sample before (PAA-start) and after (PAA-sputt.) sputtering. The positions of Ni 2p, Co 2p, and Mn 2p peaks are highlighted by dash lines in each spectrum.

Figure S18. XPS wide scans of the PAA post-mortem sample before (PAA-pm-start) and after (PAA-pm-sputt.) sputtering. The positions of Ni 2p, Co 2p, and Mn 2p peaks are highlighted by dash lines in each spectrum.